Journal of Solid State Electrochemistry (2023) 27:417–426
https://doi.org/10.1007/s10008-022-05337-1

ORIGINAL PAPER

Nonlinear dynamic behaviors of electrochemical corrosion of Ti-48Al-2Cr-2Nb alloy at high applied potentials

Xianmiao Zhang[1] · Zhijian Luo[1] · Cuijiao Liao[1]

Received: 13 July 2022 / Revised: 15 October 2022 / Accepted: 13 November 2022 / Published online: 19 November 2022

Abstract

Chronoamperometry (CA), phase space reconstruction, correlation dimension, multifractal detrended fluctuation analysis (MFDFA) combining linear sweep voltammetry (LSV), electrochemical impedance spectroscopy (EIS), and surface morphology observation were used to systematically analyze the nonlinear dynamics behavior of electrochemical dissolution of Ti-48Al-2Cr-2Nb alloy at high applied potentials. The relationships of applied potential E with nonlinear dynamic characteristic (saturation correlation dimension D_2', Hurst exponent H, the area of the spectrum S) and electrochemical corrosion parameters (capacitance ratio (C_a/C_b)) were analyzed, respectively. The results show that non-uniform corrosion at low potentials (7–13 V) results in rough surfaces; a higher potential (16 V) contributes to obtaining smoother surface. The growth of saturated correlation dimension reveals that the corrosion behavior of Ti-48Al-2Cr-2Nb alloy changes from non-uniform corrosion to uniform corrosion. The number of major variables in the electrochemical system is 6 for 7–13 V and is 7 for 16 V. The inversely proportional relationships of the area of the spectrum S and Hurst exponent H between the applied potential, respectively, testify that high potential is favorable for uniform corrosion of Ti-48Al-2Cr-2Nb alloy.

Keywords Nonlinear dynamic behaviors · Electrochemical corrosion · Phase space reconstruction · Correlation dimension · Multifractal detrended fluctuation analysis

Introduction

TiAl alloys have excellent corrosion resistance, high specific strength, and stiffness, which make them good applications in many fields, such as the turbine blade of automobiles and aero-engine [1–3]. However, their high-quality and efficient machining is a concern of researchers [4–6]. Electrochemical machining (ECM) has a great potential in machining processes of complex integral structures and high hardness materials and is a preferred machining method for TiAl alloys [3, 7–11].

In order to obtain excellent electrochemical machining condition, many researchers pay many attentions on the effects of the electro-dissolution behavior of these alloys on their machining properties using conventional electrochemical methods, such as cyclic voltammetry, linear sweep voltammetry, chronoamperometry, and electrochemical impedance spectroscopy [12–19]. The results of previous investigations have shown that the electrochemical dissolution behaviors of TiAl alloys are obviously affected by the microstructure of these alloys, the electrolyte composition, and the electrolyte temperature as well as the applied potential. There is an obvious oscillation behavior when these alloys are corroded at higher potential, high concentration electrolyte, and high electrolyte temperature. At present, the nonlinear oscillation behavior of TiAl alloys has not been studied. However, ECM is a typical electrochemical system that applies high potential [20–22], has very complex nonlinear characteristics because of the strong coupling of multiple physical fields, and presents obvious chaotic characteristics [23–25]. Moreover, two-phase TiAl alloy (γ-TiAl and α_2-Ti_3Al phase) has complex microstructures and dissolution characteristics. The above two reasons increase the difficulty of the stable and high-quality electrochemical machining of TiAl alloy [9, 26]. Electrochemical dissolution behavior is an aspect that affects the machining performance; the nonlinear behavior of current density during electrochemical dissolution is also very important aspect; it is a reflection of the evolution of electrode interface structure [21, 27, 28].

✉ Cuijiao Liao
10231@hut.edu.cn

[1] School of Mechanical Engineering, Hunan University of Technology, Zhuzhou 412007, Hunan, China

Therefore, it is indispensable to employ a nonlinear dynamic method to study complex dynamic dissolution behavior to get stable surface quality and find the optimal machining conditions. The dynamic characteristics of current density or potential in the electrochemical dissolution process can obtain a lot of detailed information about the dissolving mechanism of materials [21, 29–31]. However, previous studies focus on the simple evolutionary behavior of current or potential during electrochemical corrosion at low potentials [20, 24, 25, 32], and there are few studies about their fluctuation characteristics of dynamic corrosion behavior at high potentials, let alone systematic analysis.

In this paper, the nonlinear dynamic characteristics of chronoamperometry corrosion at high potentials of Ti-48Al-2Cr-2Nb alloy were analyzed by using nonlinear dynamics methods such as phase space construction, correlation dimension, and multifractal detrended fluctuation analysis to find the inherent law of dissolution behavior and disclose the nonlinear dynamical structure of the electrochemical systems. Electrochemical impedance spectroscopy was adopted to reveal the electrode/solution interface structure for before and after chronoamperometry corrosion. Linear sweep voltammetry (LSV) and surface morphology observation as a supplementary analysis were carried out.

Experimental

In this experiment, an ingot of as-cast Ti-48Al-2Cr-2Nb (at.%) alloy was cut into samples with the size of 5.2 mm × 5.2 mm × 10 mm, and the samples were ground by SiC sandpaper with different granularity (200, 600, 2500, and 4000 mesh) and have exposed area about 0.25 cm^2 as working electrodes of electrochemical measurement. The polished samples with 1-μm alumina polishing powder and the corroded samples were observed by scanning electron microscope (SEM, ZEISS Sigma 300) equipped with EDS in BSE and SE mode, respectively. Before observation, all samples were cleaned by ultrasonic cleaners to remove contaminants attaching to the surface and dried at 50 ℃ in the drying oven. In addition, phase identification of Ti-48Al-2Cr-2Nb alloy was performed by XRD (Ultima IV) using Cu Kα radiation (40 kV, 40 mA) for an angle range of 5–90°.

Electrochemical measurements were performed on the Bio-Logic SP150B-20A electrochemical workstation based on a three-electrode system consisting of a reference electrode (Ag/AgCl in saturated KCl), an auxiliary electrode (a large piece of Pt foil with an area of 4 cm^2), and a working electrode. To understand the dissolution behavior of Ti-48Al-2Cr-2Nb alloy, linear sweep voltammetry (LSV) (open circuit potential E_{ocp} to 16 V) with a scan rate of 100 mV/s and chronoamperometry (CA) at the potentials of 7 V, 10 V, 13 V, and 16 V for 30 s with the sampling frequency of 167 Hz were carried out in electrolyte solution (500 ml, 20 wt.% $NaNO_3$). Current density was corrected with the exposed area of each working electrode, the current density time series of CA with a length of 2^{12} (4096) for nonlinear dynamics analysis were extracted from the later stage of curves, and the length of the data is not less than 2^{10} following the effective analysis requirement of multifractal detrended fluctuation analysis (MFDFA) [33, 34]. Electrochemical impedance spectroscopy (EIS) in the frequency range of 10^{-2} to 10^5 Hz with a perturbation amplitude of 10 mV was also performed to analyze the dissolution mechanism assisting CA and LSV and to characterize interface structure. A transmission line equivalent circuit model [35] was used for the analysis of EIS in Zview software. Before measurement of EIS, open circuit potential was recorded for 2 h.

Variational mode decomposition (VMD) [36, 37] was used to reduce noise in the time series of current density before phase space reconstruction, calculation of correlation dimension, and MFDFA analysis. Electrochemical nonlinear dissolution behavior was analyzed combining nonlinear characteristic parameters of the current density with LSV, EIS, and SEM.

Results and discussions

Phases and microstructures of Ti-48Al-2Cr-2Nb alloy

Figure 1 provides the phases and microstructures of Ti-48Al-2Cr-2Nb alloy obtained by XRD and SEM in SE mode, respectively. The phase composition is more γ-TiAl phase and less α_2-Ti_3Al phase (see Fig. 1a), which verify that Ti-48Al-2Cr-2Nb alloy is two-phase alloy. The microstructure of Ti-48Al-2Cr-2Nb alloy was observed with SEM in SE mode after erosion by Kroll solution (V_{water}:V_{HF}:V_{HNO3} = 50:2:1), which illustrates Ti-48Al-2Cr-2Nb has lamellar structure (see Fig. 1b).

Electrochemical dissolution behavior

Linear sweep voltammetry

Figure 2a exhibits a linear sweep voltammetry curve. The current density experiences a stabilized region zone tending to zero (E_{ocp} to 4 V), a transition zone (4 V to 5 V), a sharp increase zone (5 V to 5.6 V), and an approximately linear growth region (5.6 V to 16 V) showing more and more evident characteristics of oscillation with the increasing potentials. It's worth noting that the stabilized region zone is composed of a passivation zone (E_{ocp} to 0 V), two transition zone (0 V to 0.4 V and 1.9 V to 2.4 V), a transpassivation zone (0.4 V to 1.9 V), and a rapid growth zone

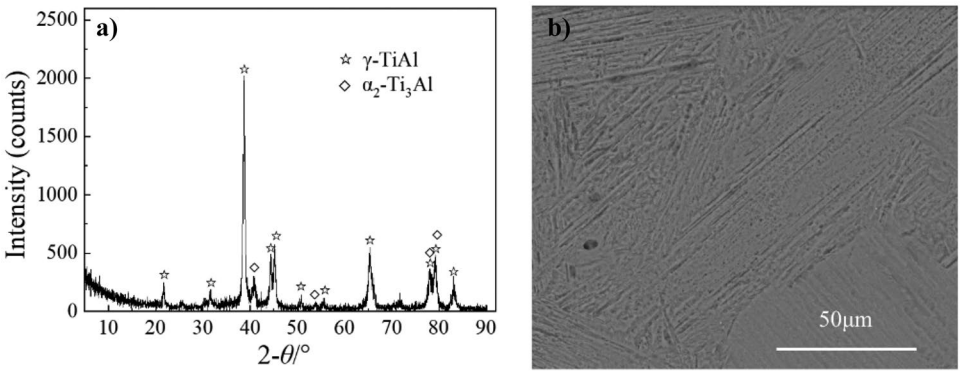

Fig. 1 Microstructures and phases of Ti-48Al-2Cr-2Nb alloy: **a** XRD and **b** SEM in BSE mode

with small oscillation (see Fig. 2b). The oscillation behavior, which is one representation of electrochemical system at large applied potential far away from the equilibrium state, is closed related with the kinetic process of electrochemical corrosion dissolution, such as adsorption, desorption, and diffusion of corrosion products, the evolution of oxidation products, and types of corrosion [20, 21, 28, 30, 31].

Chronoamperometry and denoising

Figure 3a shows the current density of chronoamperometry at different potentials. There are large fluctuations in the early and small fluctuations in the middle and later on the current density curve of each potential; the oscillation at the same time becomes more and more apparent with the increase of the applied potentials, which goes well with the above LSV. Four thousand ninety-six data points were intercepted from current density curve (see Fig. 3a, marked with a green dotted line box) to quantify the evolution behavior. Before nonlinear dynamic analysis, VMD was applied to denoise for the current density of each potential [36, 37]. The denoised time series of the current density at different potentials are exhibited in Fig. 3b and remain the inherent characteristics of the evolution of the current density.

Electrochemical impedance spectroscopy analysis

In the view of the electrochemical system, the nonlinear dynamic characteristics of current density are mainly influenced by the applied potential E and the electrode/electrolyte interface structure. Electrochemical impedance spectroscopy (EIS) before and after chronoamperometry and the fitting analysis were carried out to get information on the interface structure of the electrode/electrolyte.

The Bode plots of EIS for Ti-48Al-2Cr-2Nb alloy before and after chronoamperometry at different potentials are shown in Fig. 4a, b, respectively. In Fig. 4a, the electrochemical impedance modulus at each potential is the same shapes: a solution resistance region in the high-frequency region and a linear growth region with a similar slope in the middle- and low-frequency region. The phase angle is also similar in the evolution law: there is a sharp increase in the high-frequency region, a very slow growth in the medium-frequency region, and a rapid decline in the low-frequency region. The electrochemical impedance spectra after chronoamperometry at different potentials also have a similar structure (as exhibited in Fig. 4b). Compared to before corrosion, the impedance modulus and phase angle have a delayed increase with the decrease of the frequency, but their growth rate increases, namely, the samples after corrosion

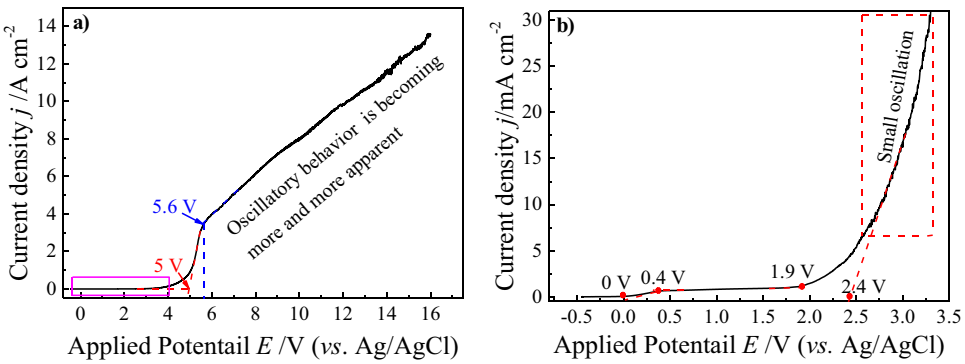

Fig. 2 **a** Linear sweep voltammetry curve of Ti-48Al-2Cr-2Nb alloy and **b** the partial enlarged drawing of **a**

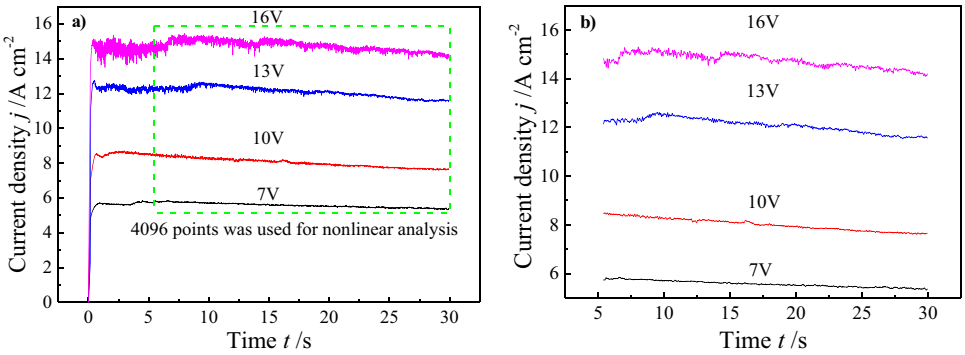

Fig. 3 **a** The time series of chronoamperometry at different potentials and **b** the denoised time series

show more obvious resistance characteristics and narrower frequency capacitive characteristics. The maximum impedance moduli decrease obviously, and the maximum-phase angle has a slight rise. Among the corroded samples, EIS of the sample after CA corrosion at 7 V differs from the other three samples.

The fitting analysis is necessary by an equivalent circuit to obtain quantitative information of electrode interface structure. A Maxwell transmission line $(R_0(RC)_6)$ (as shown in Fig. 4c) [35, 38] consisting of six RC parallel branches was used to fit all impedance spectra, where R_0 is the polarization resistance and R_i $(i = 0,\ 1,\ \ldots,\ 6)$ and $C_i = (1,\ 2,\ \ldots,\ 6)$ are adsorption resistance and adsorption capacitance of the ith electrochemical reaction, respectively. The C_b and C_a represent the sum total of C_i before and after corrosion, respectively. The fitting curves suggest that the fitting accuracy is satisfactory and the corresponding parameters are listed in Table 1.

For the same electrode system, the difference in the adsorption characteristics has closely related to the roughness of the electrode surface after corrosion associating with the dissolution behavior of the material in the corrosion process. In the case of two-phase Ti-48Al-2Cr-2Nb alloy, γ-TiAl and α_2-Ti_3Al have different dissolution characteristics. If the difference is not significant, the surface of the corroded electrode is smooth. On the contrary, it is rough. So, the capacitance ratio C_a/C_b can be used to characterize electrode coarsening after electrochemical corrosion. Figure 5 provides the change curve of C_a/C_b with the applied potential, the value of C_a/C_b increases and reaches the maximum value when the applied potential is 10 V, and then it linearly declines with the rising potential. The result suggests that the potential makes the electrode rapidly corrode and coarsen the surface, the coarsening of the electrode surface is the most serious when the potential reaches 10 V, the electrodes become smoother with the rise of the applied potential, and the error bar size of C_a/C_b has a similar variation trend with C_a/C_b value. The reasons for this shift can be attributed to the crystal structure of the Ti oxide during electrochemical corrosion of Ti-48Al-2Cr-2Nb alloy [39].

Nonlinear dynamic analysis

Phase space reconstruction and quantitative characterization

Figure 6 illustrates two-dimensional projections of phase space reconstruction and saturation correlation dimension $D_2^{'}$ at different potentials; the delay time τ is 0.042 s, 0.030 s, 0.024 s, and 0.024 s for 7 V, 10 V, 13 V, and 16 V, respectively; and the corresponding optimal m is 6, 6, 6, and 7 according to the optimization conditions $(m \geq 2\ D_2^{'} + 1)$ [40]. Two maximal eigenvalues of the vectors in phase space were

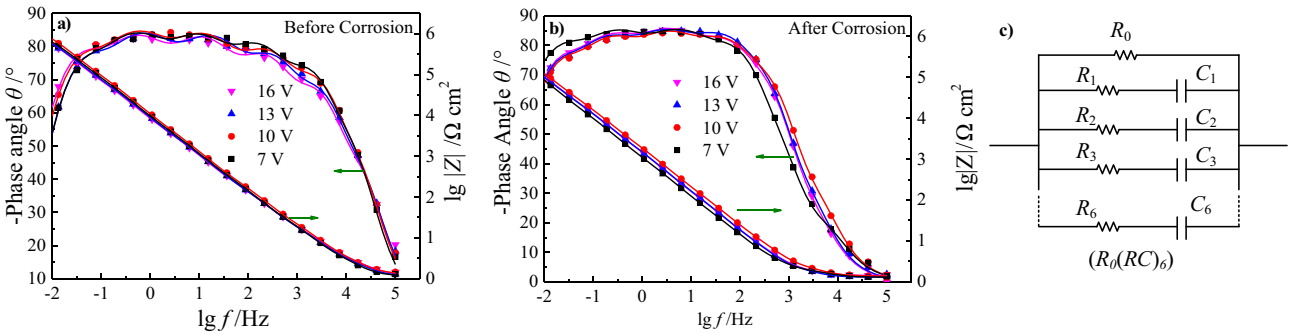

Fig. 4 The Bode plots of EIS for Ti-48Al-2Cr-2Nb alloy at different potentials: **a** before and **b** after corrosion, **c** transmission line model $(R_0(RC)_6)$

Table 1 Fitting parameters and percentage error of the transmission line equivalent circuit of EIS

	7 V		10 V		13 V		16 V	
	Before	After	Before	After	Before	After	Before	After
R_0/MΩ cm^2	1.09 (2.04)	0.36 (3.96)	1.50 (2.53)	0.36 (3.17)	0.98 (2.30)	0.31 (3.38)	1.26 (3.14)	0.32 (2.85)
C_1/μF cm^{-2}	3.42 (4.84)	4.75 (8.99)	2.44 (6.74)	7.88 (7.85)	2.34 (7.63)	0.11 (10.12)	2.21 (6.38)	7.68 (11.70)
R_1/Ω cm^2	1.50 (2.04)	3.87 (4.10)	1.78 (2.89)	3.02 (3.73)	1.67 (3.19)	3.02 (5.17)	1.79 (2.60)	4.11 (6.03)
C_2/μF cm^{-2}	3.96 (3.64)	0.44 (10.49)	3.44 (4.03)	0.43 (1.93)	4.00 (4.03)	0.60 (2.34)	4.05 (3.39)	0.58 (2.07)
R_2/Ω cm^2	6.15 (8.90)	2.83 (4.54)	5.58 (9.81)	2.74 (3.15)	4.60 (9.38)	2.43 (3.70)	5.10 (7.70)	2.35 (3.03)
C_3/μF/cm^{-2}	3.25 (4.04)	0.61 (7.24)	2.94 (4.18)	0.16 (5.59)	3.79 (4.59)	0.17 (9.86)	4.25 (3.75)	0.21 (6.50)
R_3/Ω cm^2	82.90 (9.18)	6.46 (13.55)	66.21 (9.59)	47.94 (13.55)	41.30 (10.69)	48.46 (22.18)	47.28 (8.50)	36.03 (15.20)
C_4/μF cm^{-2}	3.02 (4.79)	0.20 (4.96)	3.21 (4.02)	0.12 (5.70)	3.83 (4.55)	0.14 (6.36)	4.37 (4.05)	0.14 (5.37)
R_4/kΩ cm^2	1.31 (10.92)	0.31 (11.81)	0.84 (9.51)	0.97 (13.04)	0.51 (11.00)	1.12(13.98)	0.67 (9.40)	0.683 (13.00)
C_5/μF cm^{-2}	3.31 (4.90)	0.23 (4.68)	2.81 (5.03)	0.15 (5.32)	4.02 (4.60)	0.18 (5.69)	4.42 (4.90)	0.16 (5.02)
$R_5/\times 10^4$Ω cm^2	2.28 (11.00)	0.58 (10.19)	2.26 (11.22)	1.35 (11.00)	1.21 (10.18)	1.39 (11.64)	1.58 (10.33)	1.24 (10.27)
C_6/μF cm^{-2}	3.77 (5.00)	0.29 (4.41)	3.43 (4.93)	0.25 (4.22)	4.77 (4.69)	0.30 (4.50)	5.08 (5.08)	0.28 (3.80)
$R_6/\times 10^5$Ω cm^2	4.60 (11.24)	0.92 (9.60)	4.87 (11.04)	1.32 (8.84)	2.81 (10.62)	1.26 (9.24)	3.01 (11.80)	1.21 (7.92)
$\chi^2/10^{-4}$	2.86	1.41	3.28	1.71	4.09	1.53	4.32	1.18

selected as two vectors of the *X*-axis and *Y*-axis, respectively [41]. Figure 7a–e shows the diagrams of phase space reconstruction at different potentials. There is a strange attractor with a rodlike structure for current density at each potential [28, 30, 31], and they symmetrically distribute along the 45° diagonal line in a certain region of phase space. The length of the attractor along the 45° direction extends with the increase of the applied potentials, which represents an overall fluctuation of the current density. The width of the rodlike structure diminishes with the extension of corrosion time and arises with the increase of the potentials. Finally, the width difference of rodlike structure in the later period becomes small, which expresses the local fluctuation of current density in the corrosion process. The current density gradually becomes stable with the prolonging of corrosion time.

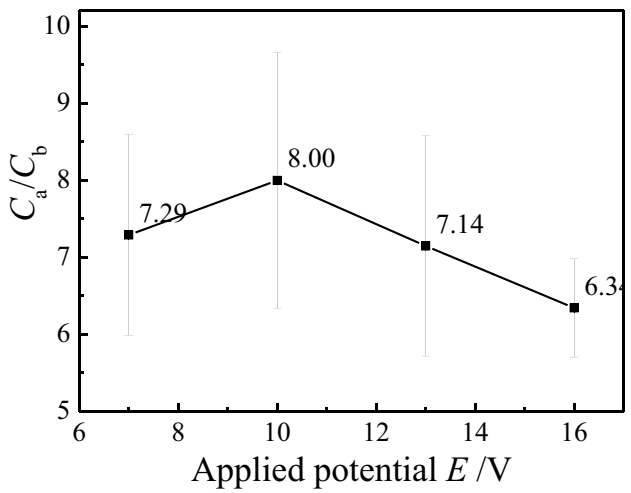

Fig. 5 C_a/C_b change curve vs. applied potential

The correlation dimension D_2 at different embedding dimensions m was calculated to quantify the structure of strange attractors. D_2 changes with m and reaches the maximum value when m is 4 or 5, namely, saturated correlation dimension $D_2^{'}$. It rises gently from 7 to 10 V and then increases rapidly from 10 to 16 V (see Fig. 6f), which suggests the corrosion behavior changes from non-uniform corrosion to uniform corrosion with the increase of the applied potentials [30, 42]. The fractal dimension of an attractor has an important physical meaning and expresses the minimum number of variables in the evolution of a corresponding dynamical system (degrees of freedom) [20–22, 30, 42, 43]. The result indicates that the electrochemical reaction becomes more and more intense, and the evolution of electrochemical system structure is more and more complex [44] with the increase of the applied potential. According to $m \geq 2\ D_2^{'} + 1$ [40] and the expansibility of strange attractor trajectories, 6 is selected as the minimum embedding dimension $m^{'}$ for 7 V, 10 V, and 13 V, and 7 is selected for 16 V, which indicates the electrochemical system at 16 V has more factors than at 7 V,10 V, and 13 V.

Multifractal detrended fluctuation analysis

Current signals in electrochemical system show obvious multifractal characteristics [45]; it has trends of some kind and is nonlinear and nonstationary [46]. Multifractal detrended fluctuation analysis shows a clear advantage in the multifractal characterization of nonlinear and nonstationary time series [34, 47–49]. It was applied to characterize multifractal features of current density at different potentials in the present work.

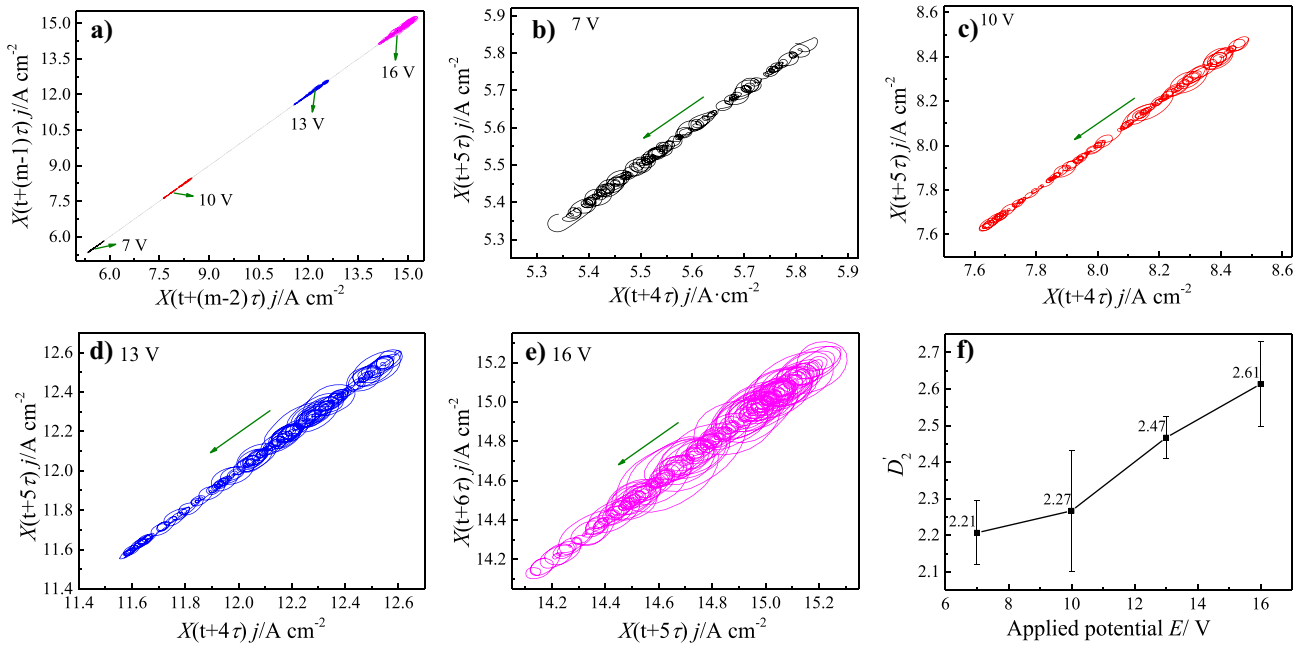

Fig. 6 **a**–**e** Phase space reconstruction and **f** saturation correlation dimension $D_2^{'}$ at different potentials

Hurst exponent H was computed based on detrended fluctuation analysis [34] when segment size s ranges from $s_{min}=16$ to $s_{min}=512$. The values of H are larger than 1.0, are less than 1.5, decline with the increase of the applied potential (7 V to 13 V), and then increase (13 V to 16 V) (see Fig. 7), which indicates that current density is nonstationary signals [34, 48, 50]. At the lower potentials (7 V and 10 V), the values of H (1.29 and 1.22) are closer to 1.5, which reveals the current fluctuation behavior at low potentials is characterized by Brown noise because of the non-uniform corrosion [34]. However, the values of H (1.12 and 1.17) at higher potentials (13 V and 16 V) are closer to 1.0, and the current density fluctuation behavior has the characteristics of 1/*f* noise [34].

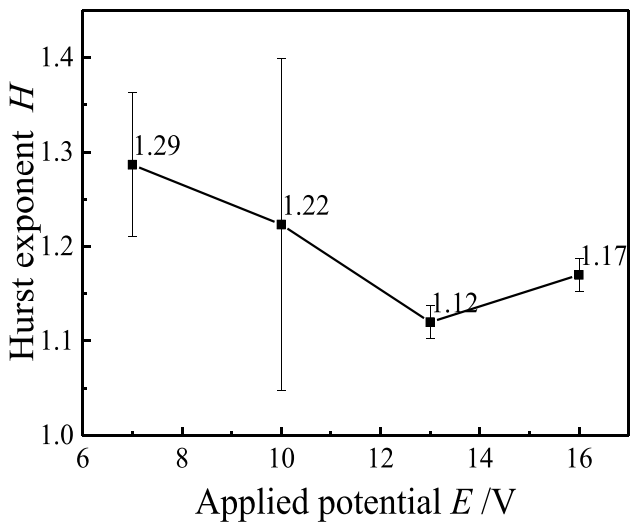

Fig. 7 Change curve of Hurst exponent H with applied potentials E

Multifractal spectrum can express some information associated with the dynamics of the current density time series. Figure 8a displays multifractal spectra $f(\alpha)\sim\alpha$ of current density at different potentials. The curves show a single hump and right-skew structures with a high level of similarity and exhibit typical features of the multifractal spectrum [51]. For the quantitative analysis, the area of the spectrum S is computed. The inverse proportional relationship between the area of the spectrum S and the applied potentials is shown in Fig. 8b. The current density time series records the amplitude of the current density fluctuation varying with time; the amplitude represents energy of the current density fluctuation [47, 52]. So we think that the area of the spectrum S of the current density time series hides total information on the energy of current density fluctuation. The inverse proportional relationship suggests that the energy of current density fluctuation decreases with the increase of the high potential, and the multifractal property of the multifractal spectrum is weakened, which prove that the two-phase Ti-48Al-2Cr-2Nb alloy is more conducive to uniform corrosion at high potentials [26].

Surface morphology observation

Surface morphology after CA corrosion at different potentials is provided as shown in Fig. 9. The corrosion

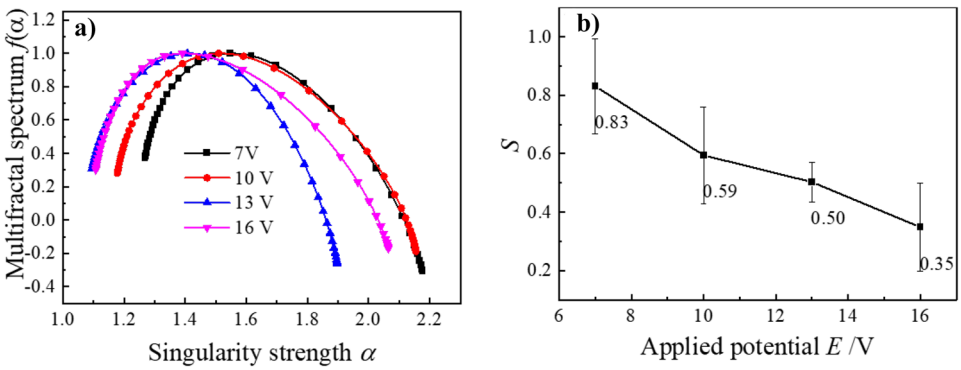

Fig. 8 **a** Multifractal spectra $f(\alpha) \sim \alpha$ and **b** the relationships between the applied potentials E and S

morphology is related to the applied potential and the microstructure of Ti-48Al-2Cr-2Nb alloy. There are three typical corrosion patterns appearing on the corroded surface at each potential: pit corrosion (marked by white arrows), selective corrosion of the lamella that is not parallel to the surface, and grain boundary corrosion (marked by red arrows) (see Fig. 9). The pit corrosion is closely related with the direction of the lamella and is manifested on the parallel surface lamella. The selective corrosion of γ-TiAl lamella attributes to the fast dissolution rate of γ-TiAl compared with α_2-Ti_3Al and is most non-evident on the corroded surface at 16 V. The grain boundary corrosion can be found on the corroded samples at 7 V and mainly appears on the corroded samples at 10 V, 13 V, and 16 V. In addition, the depth of the grain boundary corrosion is larger at 10 V and 13 V than that at 16 V (marked by red arrows) (see Fig. 9). By naked eye, it is difficult to evaluate the degree of roughness of corroded samples accurately; combined with the above result of the change curves of C_a/C_b and the applied potentials (see Fig. 5), we conclude that the high potential makes a uniform corrosion when the applied potential is higher than 10 V.

Figure 10a exhibits a cross-section of the corroded sample at 16 V with clean water and without ultrasonic cleaning. The corroded layer has large pores formed by oxygen formation and loose lamellar structures (see Fig. 10a), which are independent of the direction of the lamella. The X-ray elemental mapping images (Fig. 10b, c) verify that the corrosion layer is rich titanium, the lamellar structure is mainly α_2-Ti_3Al phase, and the γ-TiAl phase in Ti-48Al-2Cr-2Nb alloy is preferentially corroded. Figure 10d-f proves that the corroded layer consists some oxides, the Cr element almost dissolves, and the Nb element is partially soluble.

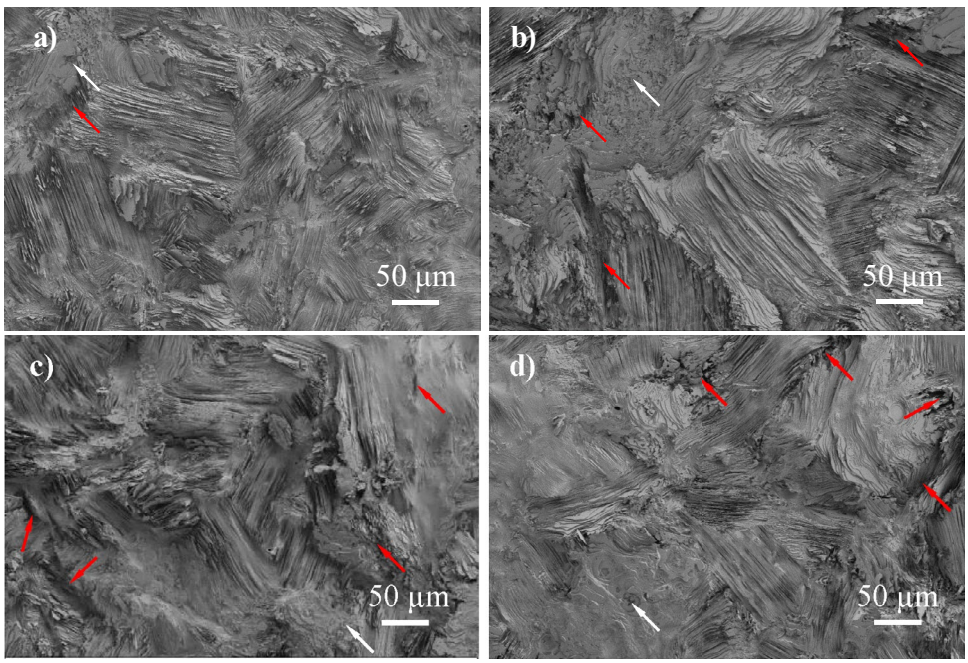

Fig. 9 SEM in SE mode of corroded surface: **a** 7 V, **b** 10 V, **c** 13 V, **d** 16 V

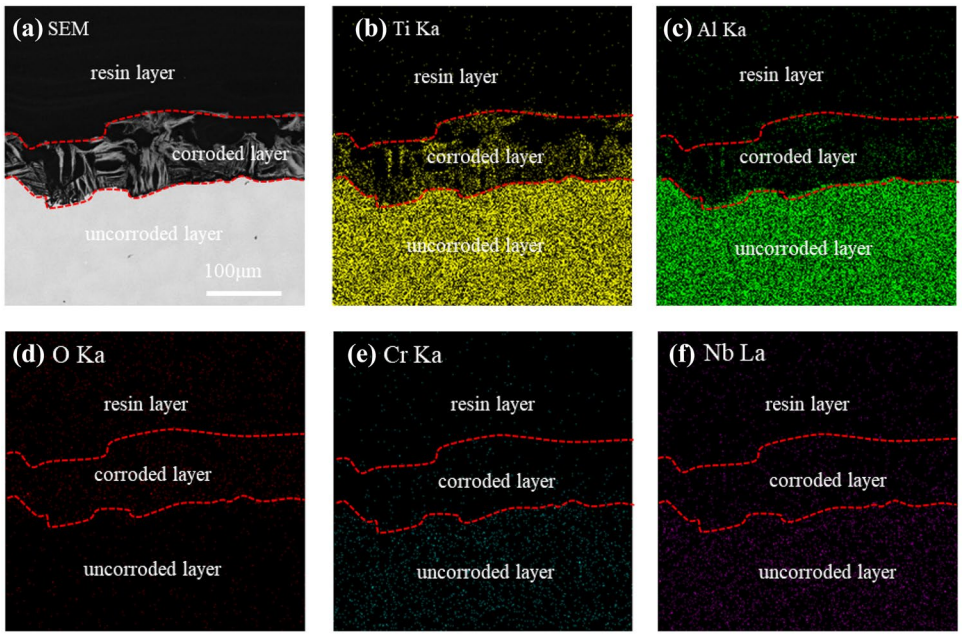

Fig. 10 **a** SEM microstructure in BSE mode and X-ray mapping of the corroded sample after CA corrosion at 16 V: **b** Ti Ka, **c** Al Ka, **d** O Ka, **e** Cr Ka, and **f** Nb La

Discussion

Two-phase Ti-48Al-2Cr-2Nb alloy consists of alternating γ-TiAl and α_2-Ti_3Al, which have different dissolution behaviors. Compared to the α_2-Ti_3Al phase, the γ-TiAl phase is preferentially corroded because of the higher content of Al (see Fig. 10a). The difference in dissolution rate between γ-TiAl and α_2-Ti_3Al is the most important factor affecting surface roughness. In addition, the dissolution behavior of special structures (such as grain boundary) is another major factor influencing the surface roughness. Capacitance ratio C_a/C_b cooperating surface morphology observation can verify the above result (see Fig. 5 and Fig. 9).

The local and global fluctuations of the current density of CA corrosion ascribe to the dissolution behavior of Ti-48Al-2Cr-2Nb alloy and electrochemical system structure. Non-uniform corrosion (for example, pit corrosion, the preferential corrosion of γ-TiAl, and grain boundary corrosion) of the alloy results in major fluctuations of current density in the earlier stage, and uniform dissolution causes small fluctuations in the later period (see Fig. 5). There are six control variables in the electrochemical system when the applied potential is not more than 13 V, and there are seven control variables when the potential is 16 V.

In general, non-uniform corrosion is more likely to occur at low potential, which results in frequent and irregular changes of current density. On the contrary, the higher the potential, the easier the uniform corrosion, and the energy of local fluctuation of the current density becomes weaken. So, the area of the spectrum S collaborating with Hurst exponent H can well reflect the evolution characteristics of the different corrosion behavior (see Figs. 8 and 7).

Conclusion

The nonlinear dynamic behavior of the current density time series of CA of Ti-48Al-2Cr-2Nb alloy was carried out from various perspectives combined with LSV, EIS, and SEM, and conclusions could be drawn as follows:

1 The surface of the corroded samples firstly coarsens with the increase of the potential (7 V to 10 V) and then becomes smoother with the increasing potential (10 V to 16 V), which testifies that a higher potential contributes to obtaining smoother surface.
2 The saturation correlation dimension with increasing applied potentials in electrochemical dissolution of Ti-48Al-2Cr-2Nb alloy reveals that the corrosion behavior of the alloy changes from non-uniform corrosion to uniform corrosion.
3 The multifractal characteristics of electrochemical dissolution of Ti-48Al-2Cr-2Nb alloy also reflect a shift in corrosion behavior.

Funding This work was supported by the National Natural Science Foundation of China (grant numbers 22072040) and the Natural Science Foundation of Hunan Province (grant number 2020JJ4271).

Declarations

Conflict of interest The authors declare no competing interests.

References

1. Burtscher M, Klein T, Lindemann J, Lehmann O, Fellmann H, Güther V, Clemens H, Mayer S (2020) An advanced TiAl alloy for high-performance racing applications. Materials 13(21):4720. https://doi.org/10.3390/ma13214720
2. Neelam NS, Banumathy S, Nageswara Rao GVS, Bhattacharjee A (2021) Study of microstructure and mechanical properties of Γ-Ti-46.5Al-2Cr-(3.5 & 5.0) Nb alloys. Mater Today 41:1069–1072. https://doi.org/10.1016/j.matpr.2020.07.131
3. Xu Z, Wang Y (2021) Electrochemical machining of complex components of aero-engines: developments, trends, and technological advances. Chinese J Aeronaut 34:28–53. https://doi.org/10.1016/j.cja.2019.09.016
4. Cakmak E, Nandwana P, Shin D, Yamamoto Y, Gussev MN, Sen I, Seren MH, Watkins TR, Haynes JA (2019) A comprehensive study on the fabrication and characterization of Ti-48Al-2Cr-2Nb preforms manufactured using electron beam melting. Materialia 6. https://doi.org/10.1016/j.mtla.2019.100284
5. Zhang Y, Lee YJ, Chang S, Chen Y, Bai Y, Zhang J, Wang H (2022) Microstructural modulation of TiAl alloys for controlling ultra-precision machinability. Int J Mach Tool Manu 174 :103851. https://doi.org/10.1016/j.ijmachtools.2022.103851
6. Feng R, Shao Z, Yang S, Cao H, Li H, Lei C, Zhang J (2022) Material removal behavior of nanoscale shear cutting and extrusion cutting of monocrystalline γ-TiAl alloy. Int J Adv Manuf Technol 119(9):6729–6742. https://doi.org/10.1007/s00170-021-08536-8
7. Wang Y, Xu Z, Zhang A (2020) Anodic characteristics and electrochemical machining of two typical γ-TiAl alloys and its quantitative dissolution model in $NaNO_3$ solution. Electrochim Acta 331:135429. https://doi.org/10.1016/j.electacta.2019.135429
8. Wang J, Xu Z, Wang J, Zhu D (2021) Anodic dissolution characteristics of Inconel 718 in C6H5K3O7 and $NaNO_3$ solutions by pulse electrochemical machining. Corros Sci 183: 109335. https://doi.org/10.1016/j.corsci.2021.109335
9. Clifton D, Mount A, Jardine DJ, Roth R (2001) Electrochemical machining of gamma titanium aluminide intermetallics. J Mater Process Technol 108:338–348. https://doi.org/10.1016/S0924-0136(00)00739-1
10. Liu W, Ao S, Li Y, Liu Z, Zhang H, Manladan SM, Luo Z, Wang Z (2017) Effect of anodic behavior on electrochemical machining of Tb6 titanium alloy. Electrochim Acta 233:190–200. https://doi.org/10.1016/j.electacta.2017.03.025
11. Malouche MM, Stein N, Lecomte J, Boulanger C, Rancic M (2020) Influence of the electrolyte composition on the electrochemical dissolution behavior of forged Inconel 718. J Appl Electrochem 50(2):197–206. https://doi.org/10.1007/s10800-019-01386-z
12. Wang Y, Xu Z, Zhang A (2019) Electrochemical dissolution behavior of Ti-45al-2mn-2nb+0.8 Vol% Tib2 Xd alloy in NaCl and $NaNO_3$ solutions. Corros Sci 157:357–369. https://doi.org/10.1016/j.corsci.2019.06.010
13. Wang Y, Xu Z, Zhang A, Xu G, Zhang C (2021) Surface morphology and electrochemical behaviour of Ti-48Al-2Cr-2Nb alloy in low-concentration salt solution. Sci China Technol Sci 64(2):283–296. https://doi.org/10.1007/s11431-019-1558-8
14. Wang Y, Xu Z, Zhang A (2019) Comparison of the electrochemical dissolution behavior of extruded and casted Ti-48Al-2Cr-2Nb alloys in $NaNO_3$ solution. J Electrochem Sci 166(12):E347–E357. https://doi.org/10.1149/2.0501912jes
15. He B, Wang D, Zhang J, Lei W (2022) Investigation of electrochemical dissolution behavior of near-α Ta15 titanium alloy in NaCl solution with low-frequency pulse current. J Electrochem Soc 169(4): 043515. https://doi.org/10.1149/1945-7111/ac669d
16. Wang H, Liu J, Gu D, Zhu D (2020) Electrochemical dissolution behavior of Ti-48Al-2Cr-2Nb in $NaNO_3$ and NaCl electrolytes. Int J Electrochem Sci 15(9):9313–9324. https://doi.org/10.20964/2020.09.70
17. Liao CJ, Liu Q, Ma XZ, Liu JH (2019) Relationship between surface heterogeneity and electrochemical interface behavior of the TiAl alloy electrode. J Phys Chem C 123(1):473–484. https://doi.org/10.1021/acs.jpcc.8b09123
18. Liao CJ, Zhang XM, Luo ZJ (2022) Magnetic field effects on electrochemical dissolution behavior and surface quality of electrochemical machining of Ti-48Al-2Cr-2Nb alloy. J Appl Electrochem. https://doi.org/10.1007/s10800-022-01756-0
19. Weinmann M, Stolpe M, Weber O, Busch R, Natter H (2015) Electrochemical dissolution behaviour of Ti90Al6v4 and Ti60Al40 used for ECM applications. J Solid State Electr 19(2):485–495. https://doi.org/10.1007/s10008-014-2621-x
20. Hudson JL, Bassett MR (1991) Oscillatory electrodissolution of metals. Rev Chem Eng 7(2):109–170. https://doi.org/10.1515/revce-1991-070201
21. Hudson JL, Tsotsis TT (1994) Electrochemical reaction dynamics: a review. Chem Eng Sci 49(10):1493–1572. https://doi.org/10.1016/0009-2509(94)85063-1
22. Baroux B, Mayet H, Gorse D (1996) Chaotic behaviors in pitting corrosion processes 97(7):461–471. https://doi.org/10.13140/2.1.4394.2087
23. Hudson JL (1993) Chaos in electrochemical systems. In Chaos in Chemistry and Biochemistry. World Scientific. https://doi.org/10.1142/9789814354745_0005
24. dos Santos CGP, Machado EG, Kiss IZ, Nagao R (2019) Investigation of the oscillatory electrodissolution of the nickel-iron alloy. J Phys Chem C 123(39):24087–24094. https://doi.org/10.1021/acs.jpcc.9b06423
25. Spanoudaki D, Kaimi A, Kouzi L, Sazou D (2018) Analysis of the temporal self-organizational phenomena observed during the electrodissolution of Zn in sulfuric acid solutions. Mater Today 5(14, Part 1):27626–27635. https://doi.org/10.1016/j.matpr.2018.09.083
26. Wang Y, Xu Z, Zhang A (2019) Comparison of the electrochemical dissolution behavior of extruded and casted Ti-48Al-2Cr-2Nb alloys in $NaNO_3$ solution. J Electrochem Soc 166:E347–E357. https://doi.org/10.1149/2.0501912jes
27. Kiss IZ, Zhai Y, Hudson JL (2002) Emerging coherence in a population of chemical oscillators. Science 296(5573):1676–1678. https://doi.org/10.1126/science.1070757
28. Eschenazi EV, Tsega Y, Ballard N, Glass G (1995) Electrochemical oscillations, surface morphology and corrosion of selected thermal sprayed alloys. MRS Proc 407:365. https://doi.org/10.1557/PROC-407-365
29. Ge X, Dietz MS, Alexander NA, Kashani MM (2020) Nonlinear Dynamic behaviour of severely corroded reinforced concrete columns: shaking table study. B Earthq Eng 18(4):1417–1443. https://doi.org/10.1007/s10518-019-00749-3
30. Legat A, Doleček V (1995) Chaotic analysis of electrochemical noise measured on stainless steel. J Electrochem Soc 142(6):1851–1858. https://doi.org/10.1149/1.2044205
31. Xia D, Song S, Wang J, Shi J, Bi H, Gao Z (2012) Determination of corrosion types from electrochemical noise by phase space reconstruction theory. Electrochem Commun 15(1):88–92. https://doi.org/10.1016/j.elecom.2011.11.032
32. Martemianov S, Thomas A, Adiutantov N, Denisov E, Evdokimov Y, Hissel D (2020) Electrochemical noise analysis of a PEM fuel cell stack under long-time operation: noise signature in the frequency domain. J Solid State Electr 24(11):3059–3071. https://doi.org/10.1007/s10008-020-04759-z

33. López J, Contreras J (2013) Performance of multifractal detrended fluctuation analysis on short time series. Phys Rev 87: 022918. https://doi.org/10.1103/PhysRevE.87.022918
34. Ihlen E (2012) Introduction to multifractal detrended fluctuation analysis in MATLAB. Front Physiol 3:141. https://doi.org/10.3389/fphys.2012.00141
35. Buteau S, Dahn D, Dahn J (2018) Explicit conversion between different equivalent circuit models for electrochemical impedance analysis of lithium-ion cells. J Electrochem Soc 165:A228–A234. https://doi.org/10.1149/2.0841802jes
36. Dragomiretskiy K, Zosso D (2014) Variational mode decomposition. IEEE Trans Signal Process 62(3):531–544. https://doi.org/10.1109/TSP.2013.2288675
37. Liu Y, Yang G, Li M, Yin H (2016) Variational mode decomposition denoising combined the detrended fluctuation analysis. Signal Process 125(C):349–364. https://doi.org/10.1016/j.sigpro.2016.02.011
38. Fletcher SBVJ, Kirkpatrick I (2014) A universal equivalent circuit for carbon-based supercapacitors. J Solid State Electr 18(5):1377–1387. https://doi.org/10.1007/s10008-013-2328-4
39. Aladjem A (1973) Anodic oxidation of titanium and its alloys. J Mater Sci 8(5):688–704. https://doi.org/10.1007/BF00561225
40. Takens F (1981) Detecting strange attractors in turbulence, in: D Rand, L-S Young (Eds.) Dynamical systems and turbulence. Warwick 1980, Springer Berlin Heidelberg, Berlin, Heidelberg
41. Bakker R, Schouten JC, Coppens MO, Takens F, Bleek C (2000) Chaotic attractor learning and how to deal with nonlinear singularities, Proceedings of the IEEE 2000 Adaptive Systems for Signal Processing, Communications, and Control Symposium (Cat. No.00EX373) 466–470
42. Aldrich C, Qi BC, Botha PJ (2006) Analysis of electrochemical noise data with phase space methods. Miner Eng 19(14):1402–1409. https://doi.org/10.1016/j.mineng.2006.01.008
43. Strozzi F, Zaldivar J (2002). Embedding theory: introduction and applications to time series analysis. https://doi.org/10.1007/978-1-4615-0931-8_2
44. Grassberger P, Procaccia I (2004) Measuring the strangeness of strange attractors, in: BR Hunt, T-Y Li, JA Kennedy, HE Nusse (Eds.). The theory of chaotic attractors, Springer New York, New York. https://doi.org/10.1007/978-0-387-21830-4_12
45. Ramírez-Platas M, Morales-Cabrera MA, Rivera VM, Morales-Zarate E, Hernandez-Martinez E (2021) Fractal and multifractal analysis of electrochemical noise to corrosion evaluation in A36 steel and AISI 304 stainless steel exposed to MEA-Co2 aqueous solutions. Chaos Soliton Fract 145 110802. https://doi.org/10.1016/j.chaos.2021.110802
46. Ashassi-Sorkhabi H, Seifzadeh D, Hosseini MG (2008) EN, EIS and Polarization studies to evaluate the inhibition effect of 3h-phenothiazin-3-one, 7-dimethylamin on mild steel corrosion in 1m HCl solution. Corros Sci 50(12):3363–3370. https://doi.org/10.1016/j.corsci.2008.09.022
47. Wang G, Ren X-m, Li L, Wang Z-Z (2007) Multifractal analysis of surface EMG signals for assessing muscle fatigue during static contractions. J Zhejiang Univ-Sc A 8(6):910–915. https://doi.org/10.1631/jzus.2007.A0910
48. Movahed MS, Jafari GR, Ghasemi F, Rahvar S (2006) Tabar MRR (2006) Multifractal detrended fluctuation analysis of sunspot time series. J Stat Mech-Theory E 02:P02003–P02003. https://doi.org/10.1088/1742-5468/2006/02/p02003
49. Kantelhardt JW, Zschiegner SA, Koscielny-Bunde E, Havlin S, Bunde A, Stanley HE (2002) Multifractal detrended fluctuation analysis of nonstationary time series. Physica A 316(1):87–114. https://doi.org/10.1016/S0378-4371(02)01383-3
50. Muzy JF, Baïle R, Bacry E (2013) Random cascade model in the limit of infinite integral scale as the exponential of a non-stationary 1/*f* noise. Application to Volatility Fluctuations in Stock Markets. Phys Rev E 87(4):042813. https://doi.org/10.1103/PhysRevE.87.042813
51. Lana X, Rodríguez-Solà R, Martínez MD, Casas-Castillo MC, Serra C, Kirchner R (2020) Multifractal structure of the monthly rainfall regime in Catalonia (NE Spain): evaluation of the non-linear structural complexity. Chaos 30(7): 073117. https://doi.org/10.1063/5.0010342
52. Wang J, Ning X, Chen Y (2003) Multifractal analysis of electronic cardiogram taken from healthy and unhealthy adult subjects. Physica A 323:561–568. https://doi.org/10.1016/S0378-4371(03)00045-1